In-situ X-ray computed tomography of decompression failure in a rubber exposed to high-pressure gas

Sylvie Castagnet, David Mellier, Azdine Nait- Ali, Guillaume Benoit

Test Method

In-situ X-ray computed tomography of decompression failure in a rubber exposed to high-pressure gas

Sylvie CASTAGNET *, David MELLIER, Azdine NAIT-ALI, Guillaume BENOIT

Institut Pprime, CNRS – ENSMA – Université de Poitiers, UPR CNRS 3346, Department of Physics and Mechanics of Materials, ISAE-ENSMA – Téléport 2, 1 avenue Clément Ader, BP 40109, 86961 Futuroscope Cedex, France

* *Corresponding author (sylvie.castagnet@ensma.fr)*

ABSTRACT

Cavitation is a damage process often observed during or after pressure release in polymers exposed to high-pressure diffusive gases. Only a few characterizations of the phenomenon have been reported in the literature, all of them being based on 2D pictures of the sample taken after removal from the pressure chamber or, more recently, inside the chamber during pressure release. This study displays the first time-resolved 3D imaging of decompression failure in high-pressure gas exposed polymers, obtained from in-situ X-ray computed tomography. New data were provided about the out-of-plane shape and volume distribution of cavities. It allowed rigorous estimation of a Morphological Representative Volume Element for the cavity field. The bias resulting from the former 2D-projection methods could be discussed.

KEYWORDS: EPDM; Hydrogen; cavitation; Representative Volume Element (RVE); cavity field

1. INTRODUCTION

Rubbers exposed to a high-pressure diffusive gas sometimes undergo cavitation or cracking during pressure release. This decompression-enhanced damage process occurs when the gas cannot desorb out of the polymer fast enough and locally expands. It has often been referred to as explosive decompression failure as most pioneer works were conducted with very fast decompression rates [1]. However, it may also occur under moderate or even slow pressure release rates, and exhibit rather slow growth kinetics.

Decompression failure was reported in the literature a few decades ago in various gas-polymer systems [2-8]. It has not been that much investigated so far, especially in hydrogen. Interest for damage resistance of high-pressure hydrogen-exposed polymers was renewed about ten years ago, when hydrogen started to be considered as a new potential energy carrier. Since decompression failure may affect permeation properties and mechanical resistance, it is a major concern for industrial components designed for fuel cell vehicles and hydrogen charge stations. A better understanding of damage mechanisms is crucial to improve the design of components and the formulation of hydrogen-exposed rubbers. It faces strong limitations, among which is hydrogen manipulation in in-situ experiments. Only

a few laboratories are able today to conduct physical and mechanical experiments under high-pressure hydrogen in polymers [9-16].

The most developed methods to track cavitation processes were based on the optical transmission of visible light in transparent samples exposed to several hydrogen pressure ranges [9, 12, 17]. By time-resolved tracking using visible light transmission through a small window machined in the front door of the chamber, Jaravel et al. [9, 14] and Kane Diallo et al. [17] studied the effect of decompression rate, saturation pressure and additional stretching on decompression failure in unfilled silicon and EPDM rubbers up to 40 MPa. Kane Diallo et al. led a statistical analysis of cavity distribution at the full-field scale (number of cavities, size distribution and spatial distribution), based on processed images of cavity fields during the decompression test. This evaluation of the spatial distribution of cavities was enriched by a covariogram method applied to each picture of the image stack. Covariogram corresponds to the probability C(h) of encountering a cavity at a distance h from another cavity along one given direction [18]. Among other data, this method allowed discussion of the features of a Morphological Representative Volume Element (MRVE) (isotropy, shape, size). MRVE data was useful for physically-motivated Finite Element modeling of the growth of pre-existing cavities on decompression in diffusive-mechanical conditions.

Visible light transmission techniques faced several strong limitations. First, these techniques were limited to transparent materials. Another limitation was the decreasing size of the window with increasing hydrogen pressure level. More importantly, these 2D techniques provided projected views of cavities through the full thickness of the sample, with possible artefacts due to overlapping, and strong assumptions about out-of-plane size and shape of cavities. In Kane Diallo et al.'s work for instance, cavities were supposed to be spherical.
X-ray computed tomography appeared an alternate method to overcome both limitations and get a 3D indirect imaging of the cavity field. The main challenge was to get good enough space resolution with a time acquisition compatible with cavity growth kinetics.
Over the last decade, X-Ray computed-tomography (CT) has become a reference nondestructive method to get indirect views of microstructure and defects in materials. Regarding polymer-based materials, it has been widely used in systems with good electronic density contrast, like between fiber and matrix in composites or between voids and polymer matrix (in foams for instance). Many studies in polymeric foams addressed the deformation and damage mechanisms under compression, first based on interrupted tests [19-22] and, more recently, during in-situ testing [23-24]
"Pure" bulk polymers are more complex systems. A first difficulty deals with the low electronic density contrast between phases: for instance, between the amorphous and crystalline layers in a semi-crystalline polymer, but also between carbon black and matrix in a filled rubber. A second difficulty is the scale of interest, usually rather fine regarding the microstructure and sometimes the defects. The size of nano-voids in a cavitated semi-crystalline polymer or the fibrils diameter in a craze are close to the best spatial resolution now reached from X-ray CT using synchrotron beam radiation.
The ex-situ X-Ray CT studies in polymers mainly addressed residual damage by mapping, either the attenuation coefficient as an indicator of the porosity level (e.g. [25] in polyvinylidene fluoride), or individualized defects (e.g. [26] about fatigue mechanisms in rubbers, [27] for the voided structure of polymer fibers).

Two major improvements resulted from the increasing access to synchrotron beam facilities over the last decade. The first was the increasing space resolution, even for ex-situ observations. This allowed imaging of smaller defects, especially in semi-crystalline polymers: micronic cavities in stretched polypropylene [28], permanent voids in necked HDPE [29], voids/fibrils microstructures in polyamide 6 [30-31], polyoxymethylene [32] or isotactic polypropylene [33]. The second interest was the ability to perform in-situ measurements during mechanical loading. Rosenberg et al. investigated the enhanced voiding in the center part of a notched specimen of polyvinylidene fluoride [25]. Poulet et al. did the same in notched samples of polyamide 11 under tension [34].
Almost all mechanical loadings applied to polymers in in-situ tomographic work were tensile tests, although the shape of samples could locally promote triaxiality. The work from Lachambre et al. in syntactic polypropylene or polyurethane foams was an exception regarding hydrostatic pressure loading [23]. Ethanol was used as the pressure fluid. Using a high-resolution X-ray tomograph in a synchrotron facility, the spatial resolution was 3.5 x 3,5 x 3.5 μm^3 with an acquisition time of 5 min. In a totally different field but with analogies regarding the damage process, Babin et al. used in-situ X-ray CT to track the expansion and coalescence of bubbles during breadmaking [35]. The average radius of bubbles was from several tens to several hundred microns. The kinetics was much slower than in the present case, with a radius rate of about 100 µm per hour.
To the authors' knowledge, the in-situ tracking of decompression failure in hydrogen-exposed polymers is reported here for the first time. This original experiment is depicted first, with special interest paid to the necessary compromise between acquisition parameters and cavity growth kinetics. Results are mainly focused on the contribution of 3D data: (i) the evaluation of the bias induced by the 2D projection of cavity field on the estimation of voided volume ratio or Morphological Representative Volume Element in visible light methods, (ii) the distribution of cavities through the thickness, (iii) the 3D anisotropy of voids.

2. EXPERIMENTAL

1. Material and decompression test

This study was carried out on a transparent unfilled EPDM used for seal applications, provided by Pr. Nishimura from Hydrogenius Laboratory at Kyushu University. Square samples (10x10 mm^2) were cut from 2 mm-thick compression-molded sheets. The diffusion coefficient D and solubility parameter S of hydrogen into the present EPDM were respectively D = 1.457 10-10 m^2/s and S = 969 wt.ppm/m3/MPa [9].
Samples were exposed to hydrogen at 12 MPa and saturated. After 150 min exposure, the pressure was released at 2.5 MPa/min.

2. X-ray Computed-Tomography

The evolution of cavitation during decompression was followed by X-ray tomography, using an Ultratom tomograph from RX Solutions® fitted with the cylindrical pressure chamber visible in Figure 1. In the present work, the chamber was filled with hydrogen (nitrogen or carbon dioxide were also possible) up to a pressure of 20 MPa. Tests were conducted at

room temperature, but the maximum possible temperature was 150°C. The device was remotely controlled; compression and decompression rates were regulated.
Inside the chamber, the sample was centered on the rotation axis, 36-mm from the X-ray source. It was scanned using a micro X-Ray source (voltage 80 kV, current 375 µA). The detector was a flat panel with 1920x1536 sensitive elements (binning mode for this study). This X-ray detector consisted of an X-ray CsI scintillator screen settled on an amorphous silicon layer. Image slices were reconstructed based on a conventional filtered back-projection algorithm.

Figure 1*: Pressure chamber for in-situ X-ray tomography of hydrogen exposure and decompression.*

Computed tomography reconstructs a 3D image of the internal structure (cavity field here) from the recording of a set of radiographs, obtained by tilting the sample at different angles. Each radiograph (i.e. for a given angle) displays a map of the local absorption of X-ray radiation. As for any transient phenomenon tracked by in-situ tomography, the present challenge was to come to a compromise between the quality of the acquired data (i.e. the stack of images used for one reconstruction) and the kinetics of the physical phenomenon. On one hand, the number of images of the stack must be large enough, and the spatial resolution small enough to ensure good quality of 3D reconstructions. Usually, the better the acquisition, the longer the time needed. On the other hand, the time elapsed between the first and the last image of the stack must be short enough to ensure slight evolution of the cavities to be reconstructed. This possible distortion effect limited the range of accessible growth kinetics. Several situations were tested to optimize the acquisition parameters. For the present decompression conditions (saturation pressure and pressure release rate), the retained configuration was a set of 200 projections, taken within 360°, acquired over a total time of 100 seconds. After reconstruction, the voxel edge size was 16µm.

Since the surfaces of the sample (initially flat) were blistered during decompression, images were cropped before segmentation. Indeed, the rubber matrix, the cavities and the surrounding medium had close grey levels. Without preliminary crop, some areas of the external medium around the blistered surface could be locally assimilated to cavities during segmentation. To avoid this, an identical number of slices was cropped from each side of the full imaged volume. The cropped volume was called “Observed Volume” in the following.
This number of slices (five) was calibrated in order to remove the blistered surface but keep the maximum volume enclosing all cavities at any time. It was defined a posteriori and kept identical for the full test, so that the resulting Observed Volume was constant all along the test (9.68 mm x 9.64 mm x 1.84 mm). However, due to swelling of the sample during decompression, the Observed Volume corresponded to a variable fraction of the real sample volume. A rigorous calculation of the voided volume ratio (which was not the aim of the present study) should be based on an updated measurement of the sample size at any time of decompression, without any crop. Again, this was not trivial because of the above mentioned difficulty of surface detection. So, in order to compare the voided volume ratio obtained from the 2D and 3D methods in section 3.1, the voided volume was divided by the initial volume of the sample in both case, making the comparison possible.
Segmentation was processed from slices along the Z direction, i.e. along the sample thickness.

3. Error estimation

A preliminary study was conducted using Matlab software® to estimate the error associated with the evolution of the cavity size during the acquisition of the stack. A numerical 3D field of perfectly spherical cavities was generated and evolved with a controlled diameter growth rate. This rate of 1µm/s was that experimentally measured in 2D by Kane Diallo et al. in the same material submitted to similar decompression conditions [17].
This numeric sample was processed in the same way as the tomographic experiment would do: virtual radiographs were computed from successive 2D projections of the numerical field, following a step-increasing tilt angle. Due to the inflation of cavities by this time, the radiographs of the stack (obtained at different angles) corresponded to slightly different values of the cavity diameter.
Two configurations were simulated. A first virtual stack of radiographs (A) was generated in "ideal" acquisition conditions, i.e. a large number of radiographs (1440 radiographs over 360°) and good spatial resolution (8x8x8 μm^3 voxel). The good reconstruction obtained from this stack A was considered as a reference. A second virtual stack of radiographs (B) was built-up in the same degraded mode as the real experiment, i.e. with a voxel size twice as large as the reference (A) and fourteen times less radiographs. The growth rate of cavities was kept unchanged for both configurations (A) and (B), as well as the time between the first and the last image of a given stack. The reconstruction algorithm was unchanged too.
The error was calculated as the number of voxels which do not belong to the same phase (cavity or matrix) between configurations A and B. For the present experimental conditions, the error was 3.2%. Compared with the repeatability of the phenomenon shown later, it could be considered as acceptable.

3. RESULTS

Figure 2 qualitatively illustrates some 3D views of the Observed Volume, obtained at different times of cavity expansion. These views showed that a non-negligible number of cavities were nucleated in the sample. With the current spatial resolution, the first ones were detected 4 minutes after the beginning of pressure release, i.e. at about 3 MPa of hydrostatic pressure. Figure 2-(c) shows the delayed nucleation of a second population of cavities, mainly clustered around the first ones, as shown in the last views of Figure 2. This phenomenon has been reported previously in the literature in other gas-rubber systems [5-6]. The delayed nucleation process made the distribution of cavities rather heterogeneous at the sample scale. Due to the inability to really measure the distance between primary and secondary cavities from 2D imaging (out-of-plane distances were not accessible), clustering has never been quantitatively investigated so far, and its origin has never been elucidated. Interaction effects between close cavities were not the purpose of the present article, but the new tomographic device presented here should open new routes to address them in the future.

Figure 2: *3D views of cavities expansion in unfilled EPDM saturated at 12 MPa and decompressed at 2.5 MPa/min (view of the Observed Volume).*

Figure 3 plots the evolution of the number of cavities and total voided volume during and after pressure release. Each graph displays three curves, corresponding to three different

tests performed with the same decompression conditions. Both graphs demonstrated the good repeatability of the method, with a maximum relative departure from the average of about 15 %. This was similar to the scatter previously obtained by Kane Diallo et al. from a 2D optical method [17].

Figure 3: *Repeatability of the (a) number of cavities and (b) total volume of cavities during three decompression tests in unfilled EPDM (exposure pressure 12 MPa; decompression rate 2.5 MPa/min) as detected from in-situ X-ray tomography.*

Compared to the former 2D methods, the present 3D tomographic one provided additional data about the thickness and the volume. The following sections focus on the bias induced by the 2D projection (inherent to the 2D optical methods) on four characteristics of single cavities or cavity fields. The contribution of in-situ tomography to each of them is detailed.

3.1 Estimation of the voided volume ratio

Tomographic reconstructions were processed to get the time evolution of the voided volume ratio, plotted in Figure 4 (red circles). The kinetics was expected to be the same as the total volume of cavities, plotted in Figure 3.
From the previous 2D visible light transmission methods, only an estimation of the voided surface ratio (i.e. a 2D projection of cavities through the thickness) could be accessed. The full cavity field was then integrated through the thickness and divided by the surface. Estimation of the volume ratio required a strong assumption about the shape of cavities (e.g. sphericity) in order to compensate the lack of out-of-plane data. Moreover, a non-negligible bias could arise from some overlapping of cavities.
In order to discuss the bias of the 2D projection estimation, the present 3D data were also processed in the same way as done from the 2D method. The cavity field was projected through the thickness of the sample. The projected voided area was calculated and the 2D surface ratio of cavities was deduced (purple triangles in Figure 4). The huge error associated with 2D projection (680% at the maximum voided state) was clearly evidenced.
As a matter of comparison, Figure 4 also displayed the 2D surface ratio measured by Kane Diallo et al. [17] in 20x20 mm samples of the same EPDM, during similar pressure release (2.5 MPa/min) but from a higher exposure pressure of 15 MPa (grey squares in Figure 4). The experimental surface ratio significantly exceeded the estimation from tomographic data. However, the exposure pressure is known to promote cavitation. The higher exposure pressure could explain the enhanced void ratio in their case. The assumption of spherical cavities (made by Kane Diallo et al. for image processing of cavity fields pictures) could also be invoked, as discussed later in section 3.3.

Figure 4: *Time evolution of the voided volume ratio obtained by in-situ X-ray tomography and projection through the thickness, for comparison purpose with the voided surface ratio obtained from 2D optical methods (* from [17]).*

3.2 Distribution of cavities through the thickness

At any decompression time, the volume of each cavity could be determined from in-situ X-ray tomography reconstructions and correlated with its location through the thickness. In each graph of Figure 5, each dot corresponds to the volume of one cavity (plotted in

micron^3) as a function of the abscissa of the gravity center in the thickness direction of the Observed Volume. The indicated time (in seconds) corresponds to the beginning of the stack acquisition.

Figure 5: *Mapping of the volume of all cavities as a function of their location through the thickness of the Observed Volume, at different times after the beginning of decompression.*

The first nucleated cavities were spread over the thickness, as observed at 200 s. The following graphs clearly evidenced that the largest cavities were located in the core of the sample. The largest cavities reached a maximum volume almost equivalent to a 700µm-diameter sphere. Many small cavities were simultaneously observed all through the thickness at any time, but with a higher concentration in the core.

3.3 Anisotropy of cavities

The visible light transmission methods available so far only displayed 2D views of cavities. In the same material as used here, Kane Diallo et al. showed that cavities were almost circular [17]. The present tomography data allowed discussion of the anisotropy of cavities in a complete 3D context. This section first focuses on the 3D morphology and anisotropy of single cavities. Anisotropy at the scale of the field will be discussed in the next section.

Figure 6*: a) view of the cavity field 3000s after the beginning of decompression and focus on the shape of one single cavity (red square) in planes (b) XY, (c) XZ) and (d) YZ.*

As a representative example, Figure 6 displays views of one single cavity extracted from the field (red square) in all planes. The isotropy of cavities in the XY plane, previously observed from the 2D method, was confirmed here, but a non-negligible flattening was clearly evidenced in the sample thickness direction. This was visible in both XZ and YZ planes, respectively, in Figure 6-(c) and (d). This result partly explained the overestimation of voided volume when calculated from the 2D surface ratio, assuming spherical cavities.

Cavity anisotropy was quantified based on the smallest convex hull, which was computed first and found very close to an ellipsoid. Three orthogonal axes were attached to each convex hull. The first axis corresponded to the maximum distance between two points of the convex hull. The second axis was orthogonal to the first one, and contained the most distant point to it on the convex hull. The third axis was obtained as the vector product of the other two directions. In case of non-uniqueness, the first occurrence was kept at each step. The anisotropy ratio of the cavity was finally defined as the ratio between the shortest and the largest axis. This ratio equalled 1 when the cavity was perfectly spherical. The above defined anisotropy ratio was very close to the Feret ratio in the present case of almost ellipsoidal cavities.

This long computational procedure has been carried out for each time and each of the three experiments. The anisotropy ratio was computed for each cavity at any acquisition time of the three experiments. Calculations were performed on the supercomputer facilities at the “Mésocentre de calcul SPIN” hosted by University of Poitiers.

Figure 7: *Time evolution of the average anisotropy ratio of cavities.*

The time evolution of the average anisotropy ratio of the cavity field was plotted in Figure 7, for one of the three tests. On average, cavities appeared more spherical at the time of maximum cavitation (maximum number and volume ratio of cavities), without reaching perfect sphericity. The flattening effect was stronger at the beginning of inflation and at the end of deflation.
However, the average anisotropy ratio only made sense depending on the shape of the distribution for the full cavity field. Then, the corresponding histograms were plotted in Figure 8 at different times after the beginning of decompression. At 200 seconds, the first population of cavities was at variable stages of the nucleation and growth process, with a highly distributed anisotropy ratio. Between 450 and 1500 seconds, histograms exhibited a major population of cavities almost spherical, with an anisotropy ratio close to 0.9. The delayed nucleation of secondary cavities was responsible for a shoulder of the main peak, visible between 300 and 800 seconds. After 200 seconds, cavities heterogeneously deflated, with again a distributed anisotropy ratio.

Figure 8: *Evolution of the distribution of anisotropy ratio at different times after the beginning of decompression (same data set as used for the average calculation in Figure 7).*

Conclusions deduced from the full cavity field were consistent with previous observations at the single cavity scale in Figure 6. Several phenomena could contribute to anisotropy. Due to the sample shape (smaller thickness than width), the diffusion boundary conditions could be anisotropic. Material anisotropy also could be incriminated, due to compression-molding of the initial rubber sheets.

3.4 Morphological Representative Volume Element

The above depicted cavity field raised the question of the size and composition of a Representative Volume Element, especially for further modelling purpose. A covariogram method can be applied to access the size of a Morphological Representative Volume Element (MRVE) of a damage field [18]. Covariogram corresponds to the probability C(h) of encountering a cavity at a distance h from another cavity along *one given direction*. A correlation length D_c can be extracted from the covariogram in any given direction. It corresponds to the distance beyond which the statistical influence of the cavity field becomes negligible in the considered direction. The correlation length D_c can be viewed as the half-size of a MRVE in the considered direction.
Kane Diallo previously applied this method to 2D-projection pictures of cavity fields [17]. Only two orthogonal directions of the sample plane (X and Y) were processed. For moderate decompression conditions, the MREV was shown to be isotropic in the sample plane, with a slightly larger width than the average size of cavities. The MRVE could be represented as a unit cell containing one or two cavities. More severe decompression conditions (i.e. fast decompression rates or high pressures for saturation) strongly promoted cavity nucleation. The MREV size drastically increased and included a large number of cavities on average. However, no information about MRVE was provided through the thickness. The evidence of two regimes had major consequences on the modeling strategy. In the former case of moderate decompression conditions, modeling could be based on a unit cell containing one

or two cavities. In the latter case of faster decompression, the MREV became very large compared to the sample size and the concept of MRVE itself was questioned, suggesting the need for alternate modeling approaches.

In the present work, covariograms were computed from the successive tomographic reconstructions (i.e. at different times) in the three main space directions: X and Y in the sample plane and Z in the thickness direction. The correlation distance D_c extracted from each covariogram was plotted in Figure 9. The time evolution of D_c along X and Y were compared to each other; this confirmed that the MRVE was almost isotropic in the sample plane all along decompression, as reported by Kane Diallo et al. from the 2D method [17]. On the other hand, the correlation length in the thickness direction Z was always smaller than in the plane direction. This meant that the MRVE was flattened in the thickness direction. This could not be detected from the 2D method.

Figure 9*: Time evolution of the correlation distances extracted from covariograms along the two principal axes in the sample plane (X and Y) and along the thickness direction (Z) during and after decompression.*

Cavitation was maximum after 600 seconds, as shown from the evolution of the number and volume ratio of cavities in Figure 3. At that time, the corresponding MRVE size was (2x0,72) x (2x0,736) x (2x0,416) mm^3 = 1.76 mm^3. This size appeared close to the average size of clusters visible in Figure 2, containing a large primary cavity surrounded by several smaller ones. An important result was that the MRVE estimated from the 3D analysis in the present decompression conditions was significantly smaller than that previously estimated in the same decompression conditions, but in a 2D context, by Kane Diallo et al. [17]. In this latter case, the MRVE size was very close to the size of the sample itself. This MRVE analysis was further proof of the bias induced by 2D projection methods. A 3D characterization of cavitation appeared essential to support modelling strategy.

CONCLUSIONS

A 3D in-situ X-ray tomography experiment was developed for better understanding of decompression failure mechanisms in gas-exposed polymers. The acquisition configuration and testing conditions were optimized to minimize artefacts and provide reliable quantitative results. A major concern of this article was to discuss and complete the alternate method used so far in the literature, i.e. the observation of 2D projections of the cavity field using visible light transmission.

In the present unfilled EPDM, the time evolution of the number of cavities was found to be similar to that measured from a 2D optical method. Even if the previously estimated surface ratio could not be directly compared to the present volume ratio, both parameters consistently evolved with time.

A major interest of this new experiment was the additional data provided in the out-of-plane direction. First, the 3D shape of cavities could be clarified. In these samples, cut from plates, cavities were not isotropic. They were flattened in the sample plane at the early stage of growth. They then became isotropic, but flattened again at the end of deflation. Regarding the out-of-plane distribution, coarser cavities were located in the core of the sample. They co-existed with a population of small cavities, spread throughout the sample thickness.

This 3D experiment also allowed complete characterization of the size and shape of a Morphological Representative Volume Element (MRVE) for the cavity field. The MRVE size was estimated from a covariogram analysis. It was also found to be flattened in the sample plane, with a size corresponding to that of clusters of primary cavity surrounded by several secondary ones. This size was much smaller than estimated from the 2D method in the same decompression conditions. This is one case of bias induced by 2D projection in the visible light transmission method.

Being able now to characterize the cavity field in 3D during decompression allows more precise investigation about key issues like the relationships between microstructure and damage resistance, or the transition from cavitation to cracking activated during pressure cycles.

ACKNOWLEDGEMENTS

This work was partially funded by the French Government programs “Investissements d’Avenir” LABEX INTERACTIFS (reference ANR-11-LABX-0017-01) and EQUIPEX GAP (reference ANR-11-EQPX-0018).

Computations have been performed on the supercomputer facilities of the Mesocentre de calcul SPIN Poitou-Charentes.

Authors are indebted to Pr. Nishimura from Hydrogenius Laboratory at Kyushu University (Japan), for kindly providing the material, and for fruitful discussions for many years now with him and members of his Research Group.

REFERENCES

[1] R. L. Denecour, A. N. Gent, Bubble formation in vulcanized rubbers, Journal of Polymer Science Part B: Polymer Physics, 6, 1853–1861, 1968.

[2] B. J. Briscoe, D. Liatsis. Internal crack symmetry phenomena during gas-induced rupture of elastomers, Rubber Chemistry & Technology, 65, 350–373, 1992.

[3] B. J. Briscoe, T. Savvas, C. T. Kelly, Explosive decompression failure of rubber: a review of the origins of pneumatic stress induced rupture in elastomer, Rubber Chemistry and Technology, 67, 384–416,1994.

[4] P. Embury. High-pressure gas testing of elastomer seals and a practical approach to designing for explosive decompression service, Sealing technology, 6, 6-11, 2004.

[5] A. N. Gent. Cavitation in rubber: a cautionary tale, Rubber Chemistry & Technology, 63, 49-53, 1990.

[6] A. N. Gent, D. A. Tompkins, Nucleation and growth of gas bubbles in elastomers, Journal of Applied Physics, 40, 2520–2525, 1969.

[7] C. W. Stewart, Nucleation and growth of bubbles in elastomers, Journal of Polymer Science Part B: Polymer Physics, 8, 937-955, 1970.

[8] A. Stevenson, G. Morgan, Fracture of elastomers by gas decompression, Rubber Chemistry & Technology, 68, 197–211, 1995.

[9] J. Yamabe, S. Nishimura, Influence of fillers on hydrogen penetration properties and blister fracture of rubber composites for O-ring exposed to high-pressure hydrogen gas, International Journal of Hydrogen Energy, 34, 1977–1989, 2009.

[10] J. Yamabe, T. Matsumoto, S. Nishimura, Application of acoustic emission method to detection of internal fracture of sealing rubber material by high-pressure hydrogen decompression, Polymer Testing, 30, 76–85, 2011.

[11] S. Castagnet, J.C. Grandidier, M. Comyn, G. Benoit, Mechanical testing of polymers into pressurized hydrogen: tension, creep and ductile fracture, Experimental Mechanics, 52, 229-239, 2012.

[12] J. Jaravel, S. Castagnet, J.C. Grandidier, G. Benoît, On key parameters influencing cavitation damage upon fast decompression in a hydrogen-saturated elastomer, Polymer Testing, 30, 811-818, 2011.

[13] A. Koga, K. Uchida, J. Yamabe, S. Nishimura, Evaluation on high-pressure hydrogen decompression failure of rubber O-ring using design of experiments. International Journal of Automotive Engineering, 2, 123-129, 2011.

[14] J. Jaravel, S. Castagnet, J.C. Grandidier, M. Gueguen, Real-time tracking and numerical simulation of cavity growth upon explosive decompression in hydrogen-saturated rubbers, International Journal of Solids and Structures, 50, 1314-1324, 2013.

[15] N.C. Menon, A.M. Kruizenga, K.J. Alvine, C. San Marchi, A. Nissen, K. Brooks, Behaviour of Polymers in High Pressure Environments as Applicable to the Hydrogen Infrastructure, ASME 2016 Pressure Vessels and Piping Conference, Vancouver, Canada, July 17–21, 2016, Volume 6B: Materials and Fabrication, Paper No. PVP2016-63713.

[16] E.R. Duranty, T.J. Roosendaal, S.G. Pitman, J.C. Tucker, S.L. Owsley, J.D. Suter, K.J. Alvine, An in situ tribometer for measuring friction and wear of polymers in a high pressure hydrogen environment., Review of Scientific Instruments, 88, 095114, 2017.

[17] O. Kane-Diallo, S. Castagnet, A. Nait-Ali, G. Benoit, J.C. Grandidier, Time-resolved statistics of cavity fields nucleated in a gas-exposed rubber under variable decompression conditions - Support to a relevant modeling framework, Polymer Testing, 51, 122, 2016.

[18] A. Nait-Ali, O. Kane-Diallo, S. Castagnet, Catching the time evolution of microstructure morphology from dynamic covariograms, Comptes Rendus de Mécanique, 343, 301-306, 2015 [English]

[19] N.P. Daphalapurkar, J.C. Hanan, N.B. Phelps, H. Bale, H. Lu, Tomography and simulation of microstructure evolution of a closed-cell polymer foam in compression, Mechanics of Advanced Materials & Structures, 15, 594-611, 2008.

[20] M.A. Di Prima, K. Gall, D.L. McDowell, R. Guldberg, A. Lin, T. Sanderson, D. Campbell, S.C. Arzberger, Cyclic compression behavior of epoxy shape memory polymer foam, Mechanics of Materials., 42, 405-416, 2010.

[21] B.M. Patterson, K. Henderson, Z. Smith, Measure of morphological and performance properties in polymeric silicone foams by X-ray tomography, Journal of Materials Science, 48, 1986-1997, 2013.

[22] S. Youssef, E. Maire, R. Gaetner, Finite element modelling of the actual structure of cellular materials determined by X-ray tomography, Acta Materialia, 53, 719-730, 2005.

[23] J. Lachambre, E. Maire, J. Adrien, D. Choqueuse, In situ observation of syntactic foams under hydrostatic pressure using Xray tomography, Acta Materialia, 61, 4035-4043, 2013.

[24] B. Patterson, N. Cordes, K. Henderson, J. Williams, T. Stannard, S. Singh, A. Ovejero, X. Xiao, M. Robinson, N. Chawla, In-situ X-ray synchrotron tomographic imaging during the compression of hyper-elastic polymeric materials, Journal of Materials Science, 51, 171-187, 2016.

[25] E. Rosenberg, N. Brusselle-Dupend, T. Epsztein, A mesoscale quantification method of cavitation in semicrystalline polymers using X-ray microtomography, Materials Science & Engineering: A, 528, 6535-6544, 2011.

[26] V. Le Saux, Y. Marco, S. Calloch, P. Charrier, Evaluation of the fatigue defect population in an elastomer using X-ray computed micro-tomography, Polymer Engineering & Science, 51, 1253-1263, 2011.

[27] T. Tanaka, K. Uesugi, A. Takeuchi, Y. Suzuki, T. Iwata, Analysis of inner structure in high-strength biodegradable fibers by X-ray microtomography using synchrotron radiation, Polymer, 20, 6145-6151, 2007.

[28] L. Farge, S. Andre, A. Pawlak, C. Baravian, S.C. Irvine, A.M. Philippe, A study of the deformation-induced whitening phenomenon for cavitating and non-cavitating semicrystalline polymers, Journal of Polymer Science- Part B: Polymer Physics, 51, 826-841, 2013.

[29] T. F. Morgeneyer, H. Proudhon, P. Cloetens, W. Ludwig, Q. Roirand, L. Laiarinandrasana, E. Maire, Nanovoid morphology and distribution in deformed HDPE studied by magnified synchrotron radiation holotomography, Polymer, 55, 6439-6443, 2014.

[30] L. Laiarinandrasana, T.F. Morgeneyer, H. Proudhon, C. Regrain, Damage of semi-crystalline polyamide 6 assessed by 3D X-ray tomography: from microstructural evolution to constitutive modeling, Journal of Polymer Science- Part B: Polymer Physics, 48, 1516-1525, 2010.

[31] N. Selles, F. Nguyen, T.F. Morgeneyer, H. Proudhon, W. Ludwig, L. Laiarinandrasana, Comparison of voiding mechanisms in semi-crystalline polyamide 6 during tensile and creep tests, Polymer Testing, 49, 137-146, 2016.

[32] J. Ricard, F. Guigne, L. Laiarinandrasana, Damage and fracture mechanisms of polyoxymethylene: Multiscale experimental study and finite element modeling, Engineering Fracture Mechanics, 115, 270-283, 2014.

[33] T.Z.N. Sokkar, K.A. El-Frahaty, M.I. Raslan, A.A. Hamza, Experimental investigation of craze morphology of isotactic polypropylene using computed tomography, Journal of Microscopy, 263, 97-105, 2016.

[34] P.A. Poulet, G. Hochstetter, A. King, H. Proudhon, S. Joannes, L. Laiarinandrasana, Observations by in-situ X-ray synchrotron computed tomography of the microstructural evolution of semi-crystalline Polyamide 11 during deformation, Polymer Testing, 56, 245-260, 2016.

[35] P. Babin, G. Della Valle, H. Chiron, P. Cloetens, J. Hoszowska, P. Pernot, A.L. Réguerre, L. Salvo, R. Dendievel, Fast X-ray tomography analysis of bubble growth and foam setting during breadmaking, Journal of Cereal Science, 2006; 43: 393-397.

FIGURE CAPTIONS

Figure 1: Pressure chamber for in-situ X-ray tomography of hydrogen exposure and decompression.

Figure 2: 3D views of cavities expansion in unfilled EPDM saturated at 12 MPa and decompressed at 2.5 MPa/min (view of the Observed Volume).

Figure 3: Repeatability of the (a) number of cavities and (b) total volume of cavities during three decompression tests in unfilled EPDM (exposure pressure 12 MPa; decompression rate 2.5 MPa/min) as detected from in-situ X-ray tomography.

Figure 4: Time evolution of the voided volume ratio obtained by in-situ X-ray tomography and projection through the thickness, for comparison purpose with the voided surface ratio obtained from 2D optical methods (* from [17]).

Figure 5: Mapping of the volume of all cavities as a function of their location through the thickness of the Observed Volume, at different times after the beginning of decompression.

Figure 6: a) view of the cavity field 3000s after the beginning of decompression and focus on the shape of one single cavity (red square) in planes (b) XY, (c) XZ) and (d) YZ.

Figure 7: Time evolution of the average anisotropy ratio of cavities.

Figure 8: Evolution of the distribution of anisotropy ratio at different times after the beginning of decompression (same data set as used for the average calculation in Figure 7).

Figure 9: Time evolution of the correlation distances extracted from covariograms along the two principal axes in the sample plane (X and Y) and along the thickness direction (Z) during and after decompression.

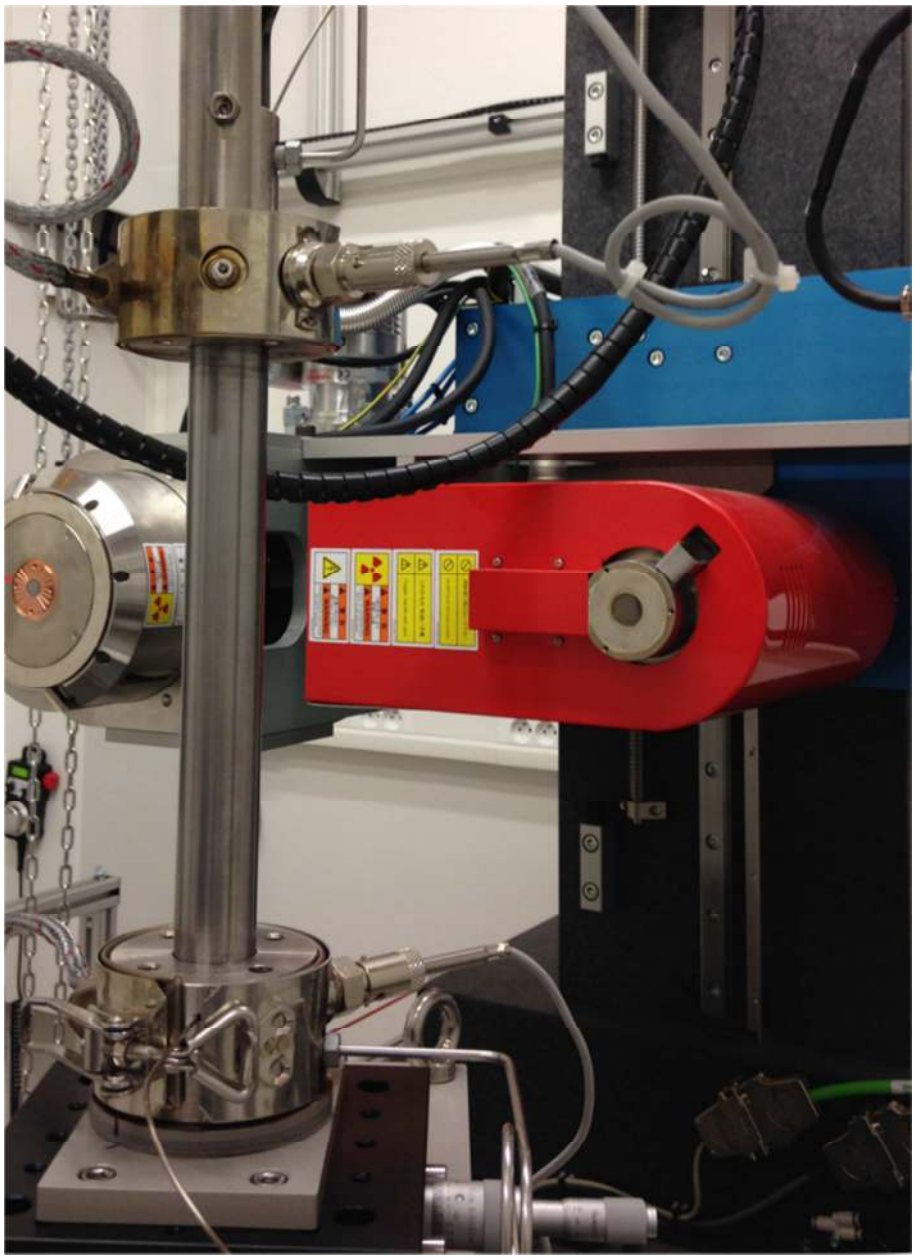

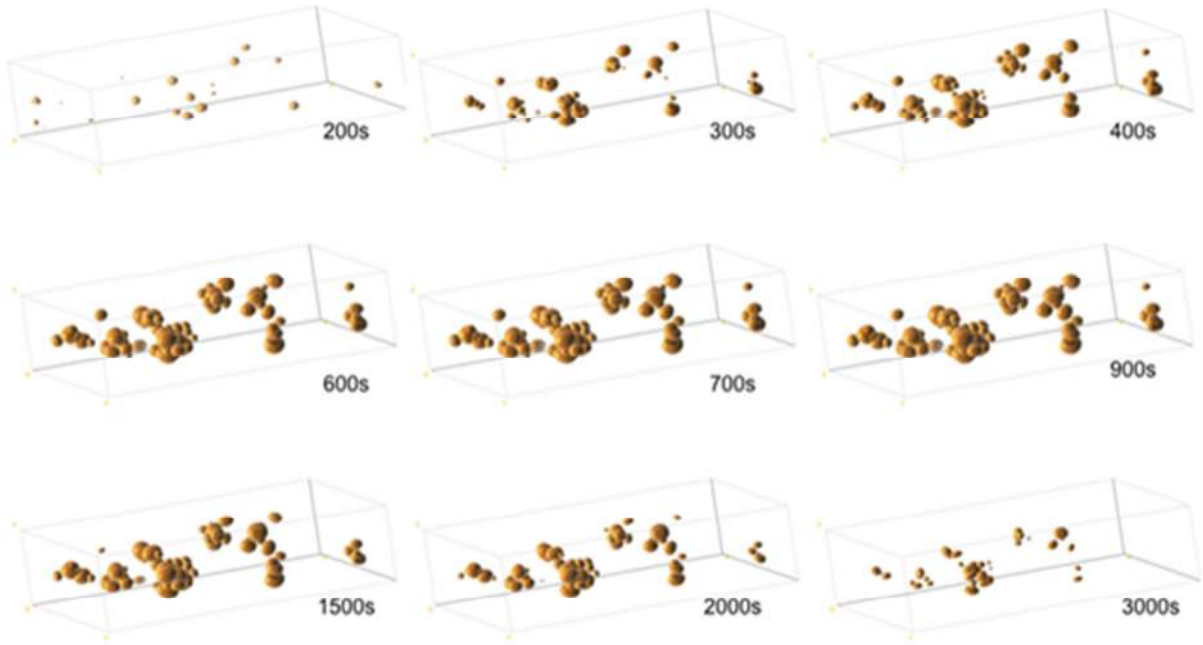
200s
300s
400s
600s
700s
900s
1500s
2000s
3000s

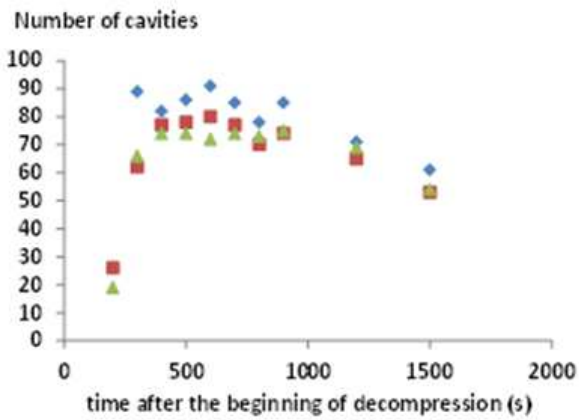
Number of cavities
100
90
80
70
60
50
40
30
20
10
0
0
500
1000
1500
2000
time after the beginning of decompression (s)

(a)

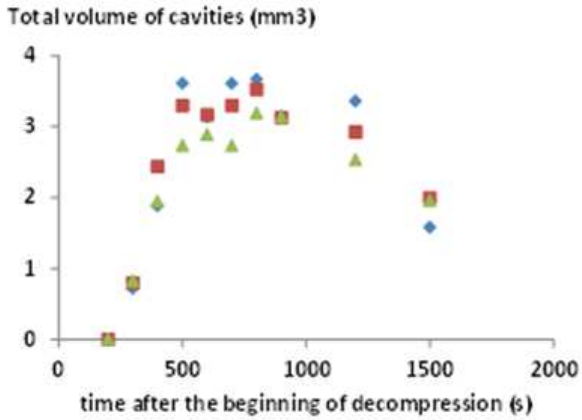
Total volume of cavities (mm3)
4
3
2
1
0
0
500
1000
1500
2000
time after the beginning of decompression (s)

(b)

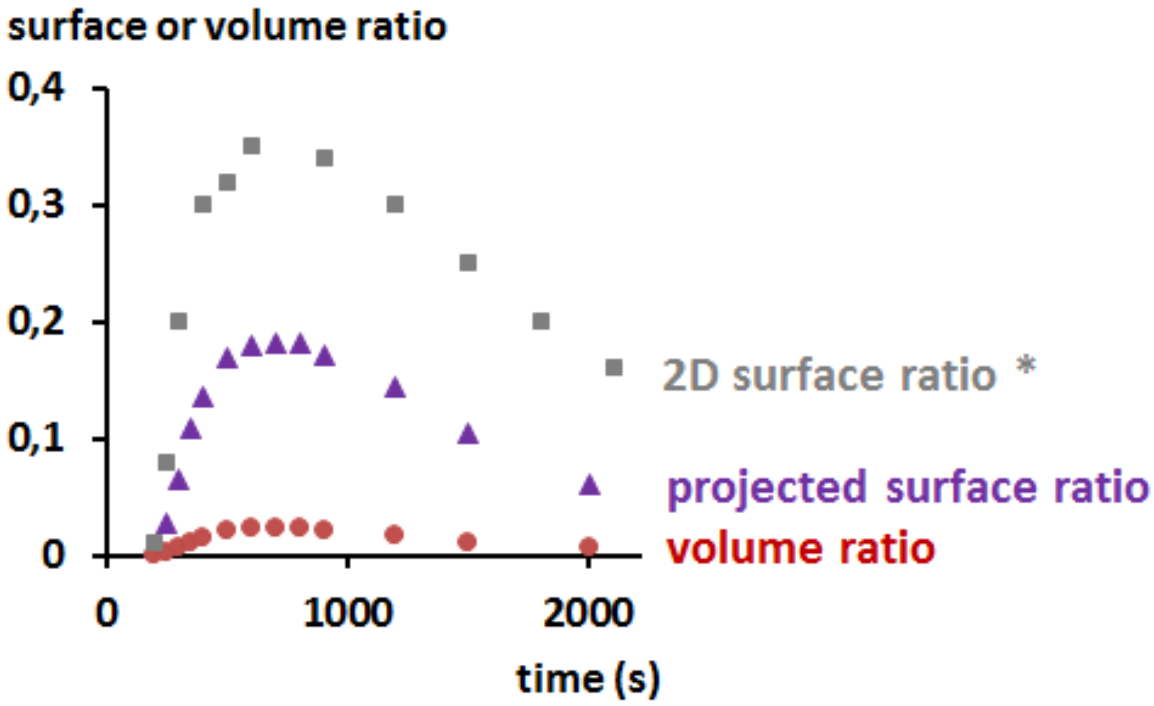
surface or volume ratio
0,4
0,3
0,2
0,1
0
0
1000
2000
time (s)
2D surface ratio *
projected surface ratio
volume ratio

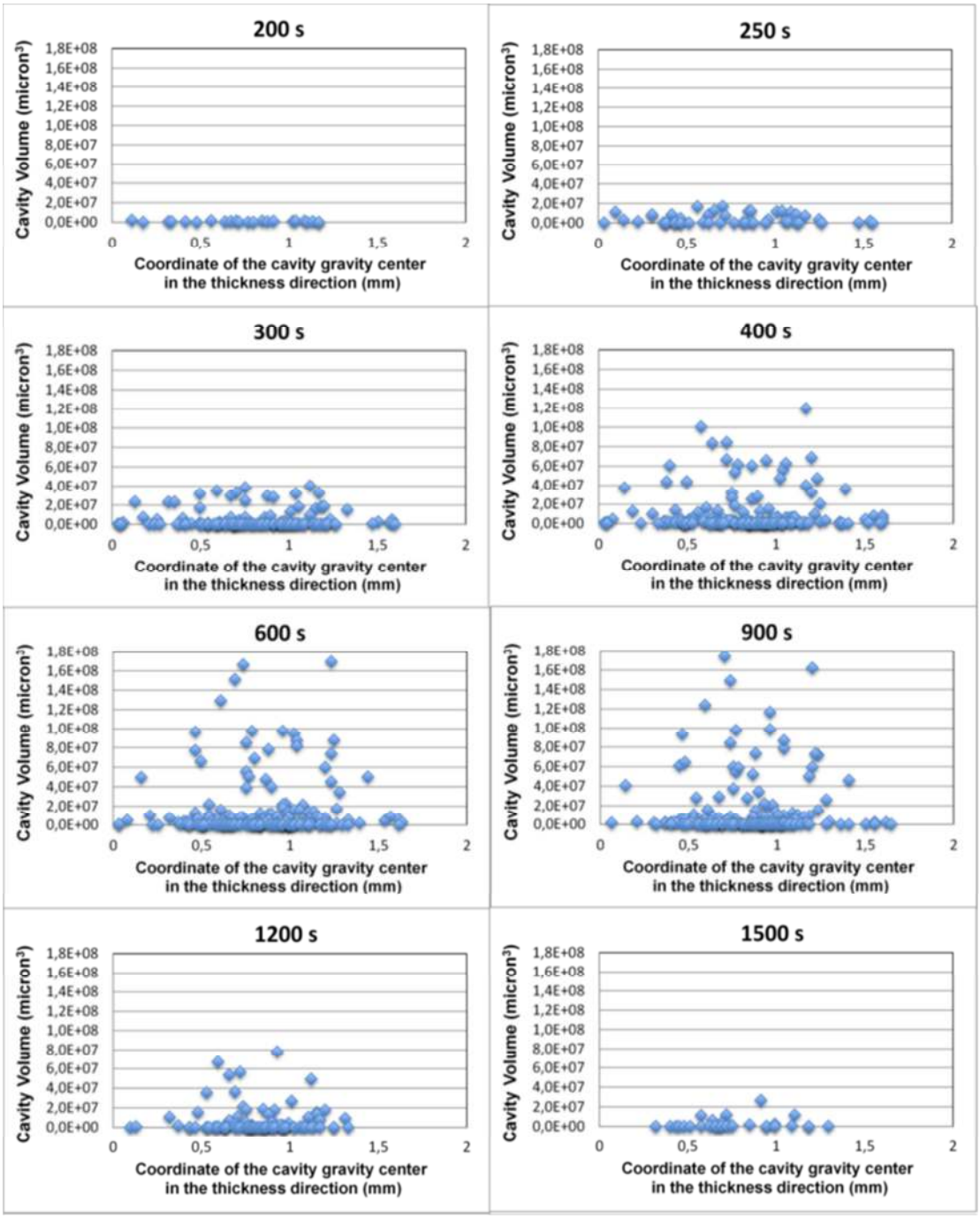
200 s
250 s
300 s
400 s
600 s
900 s
1200 s
1500 s
Cavity Volume (micron³)
1,8E+08
1,6E+08
1,4E+08
1,2E+08
1,0E+08
8,0E+07
6,0E+07
4,0E+07
2,0E+07
0,0E+00
0
0,5
1
1,5
2
Coordinate of the cavity gravity center in the thickness direction (mm)

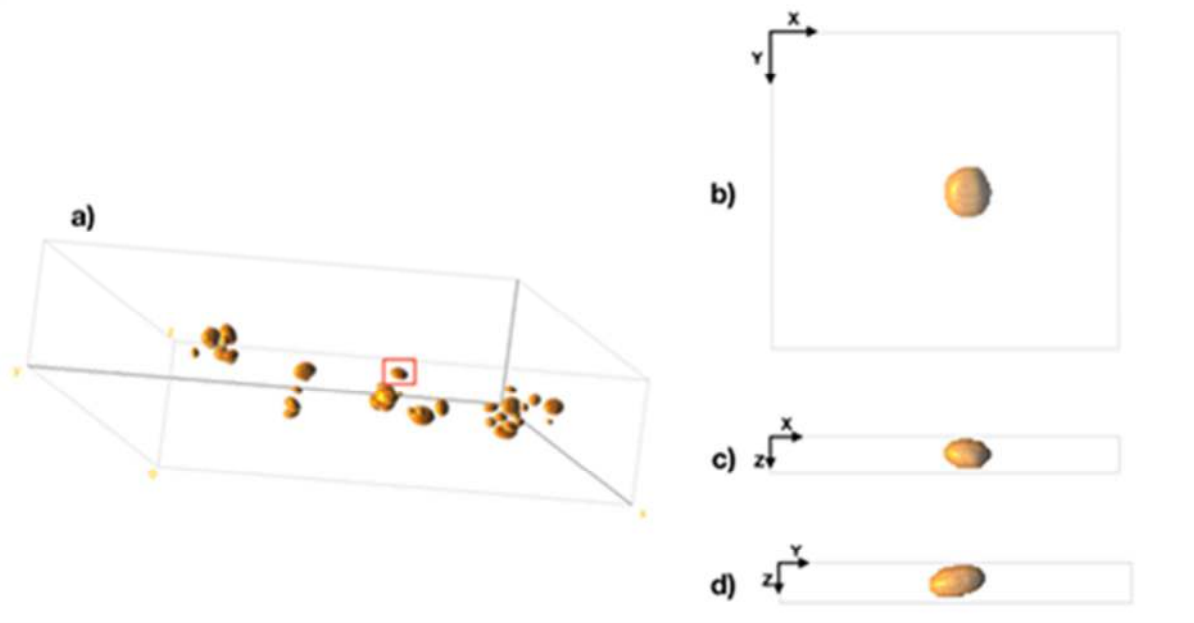
a)
b)
X
Y
c)
X
Z
d)
Y
Z

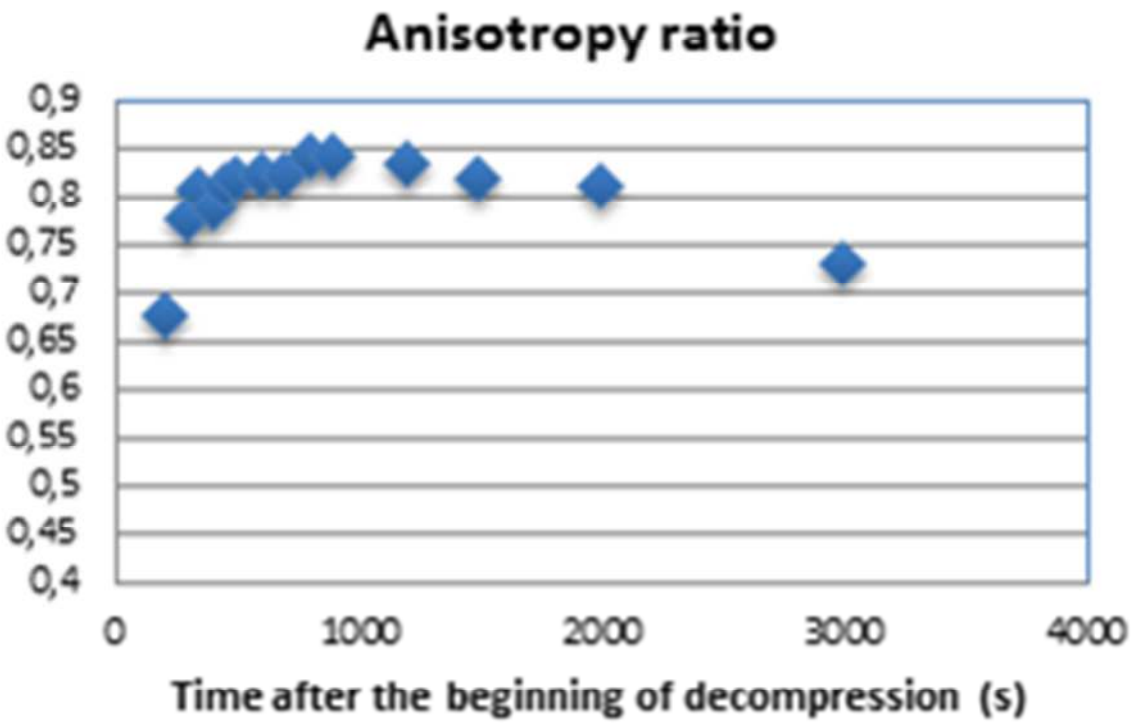
Anisotropy ratio
0,9
0,85
0,8
0,75
0,7
0,65
0,6
0,55
0,5
0,45
0,4
0
1000
2000
3000
4000
Time after the beginning of decompression (s)

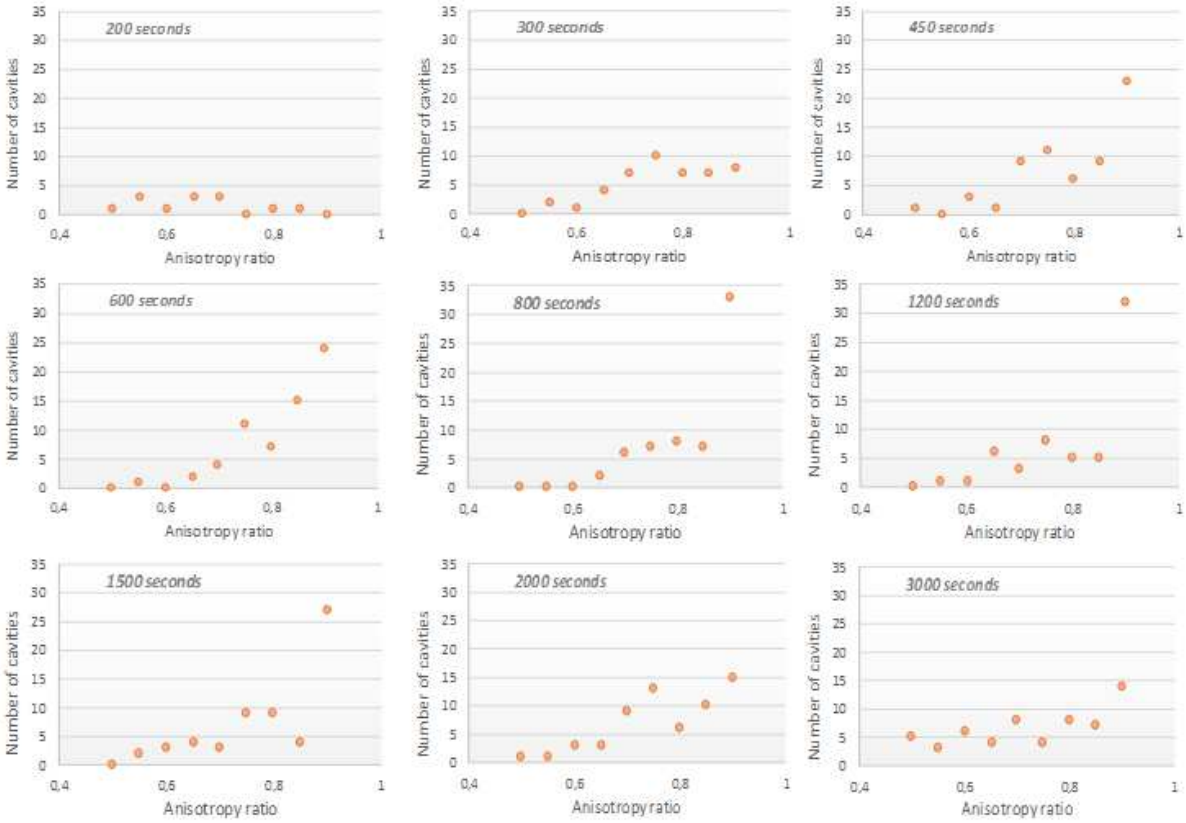
200 seconds
300 seconds
450 seconds
600 seconds
800 seconds
1200 seconds
1500 seconds
2000 seconds
3000 seconds
Number of cavities
Anisotropy ratio
0
5
10
15
20
25
30
35
0,4
0,6
0,8
1

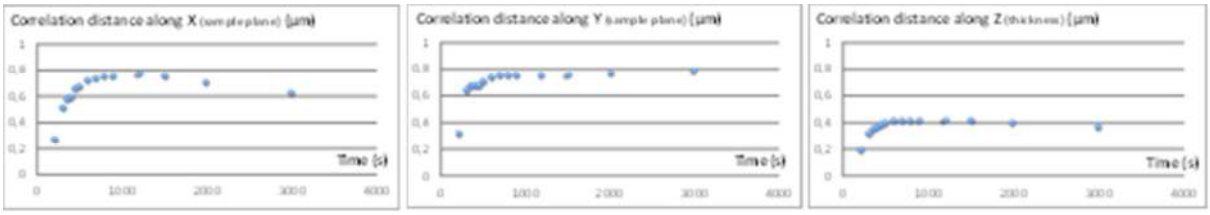
Correlation distance along X (sample plane) (µm)
Time (s)
Correlation distance along Y (sample plane) (µm)
Time (s)
Correlation distance along Z (thickness) (µm)
Time (s)

HIGHLIGHTS

Time-resolved 3D views of decompression failure in rubbers are reported for the first time.

An EPDM, exposed to high-pressure hydrogen, was tracked by in-situ computed tomography.

Novel and quantitative data were provided about the out-of-plane morphology and volume distribution of cavities.

Some bias, induced by 2D projection in the former visible light transmission methods, were discussed.

The experiment opens new routes for a better understanding and accurate quantification of decompression failure.